MRS Advances
https://doi.org/10.1557/s43580-026-01667-8

ORIGINAL PAPER

Comparative study of Ni–CeO_2 catalysts prepared by impregnation and coprecipitation for CO_2 methanation

Nobuko Fukuda[1] · **Shuichi Imano**[1] · **Nozomi Nakahara**[1]

Received: 20 November 2025 / Accepted: 24 April 2026

Abstract

This study explores how synthesis methods affect the structure and CO_2 methanation performance of Ni–CeO_2 catalysts prepared by coprecipitation and impregnation under identical conditions. Coprecipitation generated particles below 100 nm with uniform elemental distribution, together with large bulk-like particles exhibiting locally concentrated Ni species, attributed to differences in hydroxide solubility. Impregnation, by contrast, produced very large particles (> 500 nm) with smaller particles attached, while maintaining relatively homogeneous elemental distribution. Coprecipitated catalysts showed slightly higher surface area and oxygen vacancy concentration, resulting in higher apparent turnover frequencies (TOF_{app}) below 300 °C due to enhanced CO_2 adsorption and high Ni site density. However, at temperatures above 350 °C, impregnated catalysts displayed higher CH_4 selectivity and TOF_{app}, indicating reduced kinetic limitations and more efficient active-site utilization. These results provide insights for rational design of efficient CO_2 methanation catalysts.

Introduction

In recent years, emissions of carbon dioxide (CO_2) and other greenhouse gases have continued to rise. This rapid increase is driving global warming and related environmental issues, including extreme weather events, acid rain, shifts in animal migration, food supply imbalances, and disturbances in ecosystem nutrition. To minimize atmospheric CO_2 emissions, it is essential to explore renewable energy sources, capture and store CO_2, or convert CO_2 into valuable products. Among the various processes for converting CO_2 into sustainable products, CO_2 methanation has attracted significant attention.

Methanation is a technology that can supply methane (CH_4) as an alternative fuel to natural gas and as a chemical feedstock, thereby supporting the chemical industry. Globally, the goal is to achieve carbon neutrality by 2050, aiming for zero net greenhouse gas emissions across society. As a solution, incorporating methanation into the carbon cycle and replacing natural gas—the raw material for city gas—with synthetic methane is proposed to effectively achieve net-zero CO_2 emissions. In this system, surplus electricity from renewable energy sources can be efficiently stored by converting it into hydrogen (H_2) and CH_4, which is expected to accelerate the widespread adoption of renewable energy [1]. Thus, methanation plays a crucial role not only in supporting the chemical industry but also in maximizing renewable energy utilization, reducing greenhouse gases, and efficiently storing energy. Therefore, the development value of methanation technology is high, and extensive research is being conducted across various fields, such as materials and processes, from both industrial and academic perspectives.

Methanation via CO_2 reduction proceeds through the following Sabatier reaction:

$$CO_2 + 4H_2 \rightarrow CH_4 + 2H_2O.$$

This reaction can occur at lower temperatures in the presence of a catalyst. Ruthenium is a metal with high catalytic activity for methanation, but its high-cost limits industrial application [2]. Nickel (Ni), while less active than ruthenium, offers high reaction selectivity and is a practical catalyst for industrial applications due to its lower cost [3]. The support for the catalyst metal is also crucial for activity. Besides providing a high surface area, it functions as a promoter that activates the catalyst metal through interaction [4]. Cerium oxide (CeO_2) can enhance Ni activity as a CO_2 reduction catalyst because of its facile interconversion between Ce^{4+} and Ce^{3+} oxidation states [5–13]. Beyond

✉ Nobuko Fukuda
n-fukuda@okayama-u.ac.jp

[1] Graduate School of Environmental, Life, Natural Science and Technology, Okayama University, 3-1-1 Tsushima-Naka, Kita-Ku, Okayama 700-8530, Japan

Published online: 11 May 2026

methanation, cerium oxide also exhibits high activity in other reactions, such as hydrogenation of nitro groups in aromatics [14] and synthesis of γ-butyrolactone via reduction of maleic anhydride [15]. The oscillation of valence states appears to enable flexible interaction with Ni while regulating oxygen vacancies and oxygen storage capacity [16].

In preparing nickel–cerium oxide (Ni–CeO_2) catalysts, impregnation and coprecipitation are common methods. In the typical coprecipitation method, Ni and Ce nitrates are mixed and co-precipitated as hydroxides in a strong alkaline aqueous solution, followed by heating in air to convert them into oxides, and finally reducing nickel oxide (NiO) under hydrogen to metallic Ni. This approach easily creates catalytic active sites due to oxygen vacancies from Ni^{2+} doping into the CeO_2 structure. However, if the interaction between Ni and Ce species is too strong, NiO reduction may be inhibited. In the impregnation method, pre-synthesized CeO_2 particles are immersed in an aqueous nickel salt solution, allowing adsorption onto the CeO_2. The material is then heat-treated under hydrogen to reduce the Ni species to metallic Ni. This method simplifies adjustment of nickel loading and preparation, but the amount of nickel ion doping is lower than in coprecipitation, raising concerns about fewer oxygen vacancies serving as active sites.

In this study, Ni–CeO_2 catalysts prepared by coprecipitation and impregnation were investigated under strictly identical conditions, including a Ni loading of 20 wt.% as well as calcination at 500 °C and hydrogen reduction at 600 °C, in order to elucidate differences in their structure and chemical states and to examine their effects on methanation behavior at various temperatures.

Materials and methods

Materials

Potassium hydroxide (KOH), cerium(III) nitrate hexahydrate ($Ce(NO_3)_3{\cdot}6H_2O$), and nickel (II) nitrate hexahydrate ($Ni(NO_3)_2{\cdot}6H_2O$) were purchased from FUJIFILM Wako (Osaka, Japan).

Catalyst preparation by coprecipitation method

A total of 290 mL of 0.2 M $Ce(NO_3)_3$ aqueous solution and 170 mL of 0.2 M $Ni(NO_3)_2$ aqueous solution were added to 2.7 L of 0.2 M KOH aqueous solution. The mixture was magnetically stirred for 24 h at room temperature. The resultant precipitate was collected by filtration, dried in air at 110 °C for 24 h, and then calcined in air at 500 °C for 5 h. Subsequently, it was reduced under an H_2 atmosphere at 600 °C for 6 h to obtain CeO_2 loaded with 20 wt% Ni (co-Ni–CeO_2).

Catalyst preparation by impregnation method

First, 290 mL of 0.2 M $Ce(NO_3)_3$ aqueous solution was added to 870 mL of 0.2 M KOH aqueous solution, and the mixture was magnetically stirred for 24 h at room temperature. The precipitate obtained by filtration was dried in air at 110 ℃ for 24 h and calcined in air at 500 ℃ for 5 h. The resulting CeO_2 powder was then mixed with 0.2 M $Ni(NO)_3$ aqueous solution, and the solvent was evaporated. The amount of $Ni(NO_3)_2$ solution was adjusted so that the weight of zero-valent Ni corresponded to 20 wt.% of the CeO_2 weight. The sample was calcined in air at 500 ℃ for 5 h, and subsequently reduced under an H_2 atmosphere at 600 ℃ for 6 h to obtain CeO_2 loaded with 20 wt.% Ni (imp-Ni–CeO_2).

Characterization

Powder X-ray diffraction (XRD) patterns were recorded using a Rigaku RINT 2100 with a step size of 0.02° (Cu Kα radiation: $\lambda = 0.154$ nm). Curve fitting was performed on selected diffraction peaks using the Lorentz function. Crystal planes were identified using the JSPDS database. Crystallite size (D) was estimated using the Scherrer equation (Eq. 1):

$$D = \frac{K\lambda}{\beta \cos\theta} \tag{1}$$

where K is the Scherrer constant, λ is the X-ray wavelength, β is the peak broadening, and θ is the Bragg angle. Scanning transmission electron microscopy (STEM) was performed using a Hitachi SU9000 at an acceleration voltage of 30 kV. Elemental mapping for Ni, Ce, and O was obtained using an energy-dispersive X-ray (EDX) detector. Nitrogen adsorption measurements at liquid nitrogen temperature were carried out using a Gemini 2375 (SHIMADZU). Specific surface area was calculated by the Brunauer–Emmett–Teller (BET) method. X-ray photoelectron spectroscopy (XPS) was performed using a Quantes (ALVAC-PHI) instrument with a monochromatic Al Kα source (1486.6 eV). Binding energy was calibrated using the C1s peak at 284.8 eV. Spectra were analyzed using MultiPak 9.9.3 and XPSPEAK 4.1.

Methanation test

Catalyst performance was evaluated at 200–400 °C in a fixed-bed quartz tubular reactor containing 1 cm^3 of catalyst at a gas hourly space velocity (GHSV) of 1800 h^{-1}. The feed gases (N_2, H_2, and CO_2) were controlled by a KOFLOC mass flow controller to achieve a molar ratio of N_2:H_2:CO_2 = 35:12:3 and a total flow rate of 100 mL/min. Temperature was controlled using a CHINO KP 1000 with

measurements taken every 50 °C from 200 °C for 40 min. Products formed after 30 min at each temperature were analyzed by gas chromatography (SHIMADZU GC-8AID) equipped with a thermal conductivity detector (TCD). Catalyst performance was evaluated based on CO_2 conversion and CH_4 selectivity.

The apparent turnover frequency (TOF_{app}) was estimated using the fraction of metallic Ni obtained from XPS analysis, together with the CO_2 conversion (X_{CO2}), CH_4 selectivity (Y_{CH4}), and the molar flow rate of CO_2 at each temperature, F_{CO2} [mol s^{-1}], obtained from the methanation tests. TOF_{app} was defined by the following equation [8]:

$$\mathrm{TOF_{app}}\left[s^{-1}\right] = \frac{F_{CO2} \times X_{CO2} \times Y_{CH4}}{n}$$

Here, the number of effective active sites for CO_2 methanation, n, was approximated by assuming that all surface metallic Ni species participate in the reaction, as given by

$$n \approx n_{\mathrm{Ni,total}} \times f_{\mathrm{Ni^0,XPS}}$$

where $n_{\mathrm{Ni,total}}$[mol] represents the total amount of Ni in the catalyst and $f_{\mathrm{Ni^0,XPS}}$ denotes the fraction of metallic Ni determined by XPS analysis. Accordingly, TOF_{app} can be approximated as

$$TOF_{app} \approx \frac{F_{CO2} \times X_{CO2}}{n_{Ni,total} \times f_{Ni^0,XPS}}\left[s^{-1}\right] \quad (2)$$

Results and discussion

Crystallization behaviors during each preparation process

Figure 1A, B presents the XRD patterns obtained during the preparation processes to imp-Ni–CeO_2 and co-Ni–CeO_2, respectively. To facilitate peak identification, an arbitrary scaling factor was applied to the vertical axis. For the impregnation method, the diffraction pattern after impregnation of CeO_2 with $Ni(NO_3)_2$ solution followed by calcination at 500 °C (Fig. 1A(b)) exhibited peaks corresponding to NiO (111), (200), and (220), sequentially from the lower angles. After reduction under H_2 atmosphere (Fig. 1A(c)), NiO peaks disappeared and metallic Ni peaks emerged, confirming NiO reduction. CeO_2 peaks were consistently observed, and their half-widths decreased significantly as the process progressed, indicating crystallite growth and enhanced crystallization during heating at 600 °C.

For the coprecipitation method, the dried coprecipitate displayed a $Ni(OH)_2$ peak (Fig. 1B(a)). After calcination at 500 °C, CeO_2 peak intensity increased, $Ni(OH)_2$ peak disappeared, and NiO peak appeared (Fig. 1B(b)). Subsequent reduction under H_2 eliminated NiO peaks and introduced metallic Ni peaks (Fig. 1B(c)). Regarding cerium species, the dried sample exhibited broad CeO_2 peaks without distinct hydroxide peaks. Previous XRD studies (André et al. [17]) indicate that cerium hydroxide gradually oxidizes in air, forming CeO_2 via $CeO_x(OH)_{3-x}$, intermediates, whose peaks overlap with CeO_2, explaining the broad half-width observed. Given that drying occurred at 110 °C in air, partial oxidation to CeO_2 is plausible. After calcination at 500 °C, CeO_2 peak half-widths decreased, suggesting further oxidation and crystallization. Heating at 600 °C under H_2 further narrowed CeO_2 peaks, similar to the impregnation method. To compare Ni species crystallization, NiO (111) and Ni (111) peaks were extracted from Fig. 1A and B and plotted in Fig. 1C and D, respectively. Crystallite sizes calculated from peak widths using Eq. 1 are summarized in the table in Fig. 1. NiO crystallites prepared by impregnation were approximately 1.6 times larger than those from coprecipitation, likely because impregnation introduces $Ni(NO_3)_2$ onto preformed CeO_2, minimizing interference from Ce species during NiO formation. Similarly, metallic Ni crystallites obtained after reduction were larger for the impregnation method.

Elemental distribution in the catalysts

Figure 2 presents STEM images, elemental mapping with EDX, and particle size distribution histograms of imp-Ni–CeO_2 and co-Ni–CeO_2 catalysts. For imp-Ni–CeO_2 (Fig. 2A), agglomerates are observed in which particles smaller than 100 nm are attached to particles larger than 500 nm, suggesting that particle growth occurred during multiple calcination steps, leading to an overall increase in particle size. Elemental mapping indicates that Ce, Ni, and O are relatively uniformly distributed, implying that Ni species are well dispersed on the surfaces of CeO_2 particles of various sizes. In contrast, co-Ni–CeO_2 (Fig. 2B) exhibits regions dominated by agglomerated particles smaller than 100 nm, as well as regions consisting of agglomerates of plate-like particles larger than 500 nm or particles exceeding 100 nm. According to the elemental maps, Ce, Ni, and O are uniformly distributed in the regions where small particles (< 100 nm) are aggregated, whereas Ni species are locally enriched in regions where larger particles are present. For imp-Ni–CeO_2, the uniform elemental distribution is attributed to the impregnation process in $Ni(NO_3)_2$ aqueous solution, during which Ni species are homogeneously adsorbed onto the CeO_2 surface prior to calcination. In contrast, the co-Ni–CeO_2 catalyst is considered to consist of two types of particles: relatively small particles with homogeneous elemental distributions formed by the coprecipitation of $Ce(OH)_3$ and $Ni(OH)_2$, and coarser particles with segregated elemental distributions resulting from the sequential

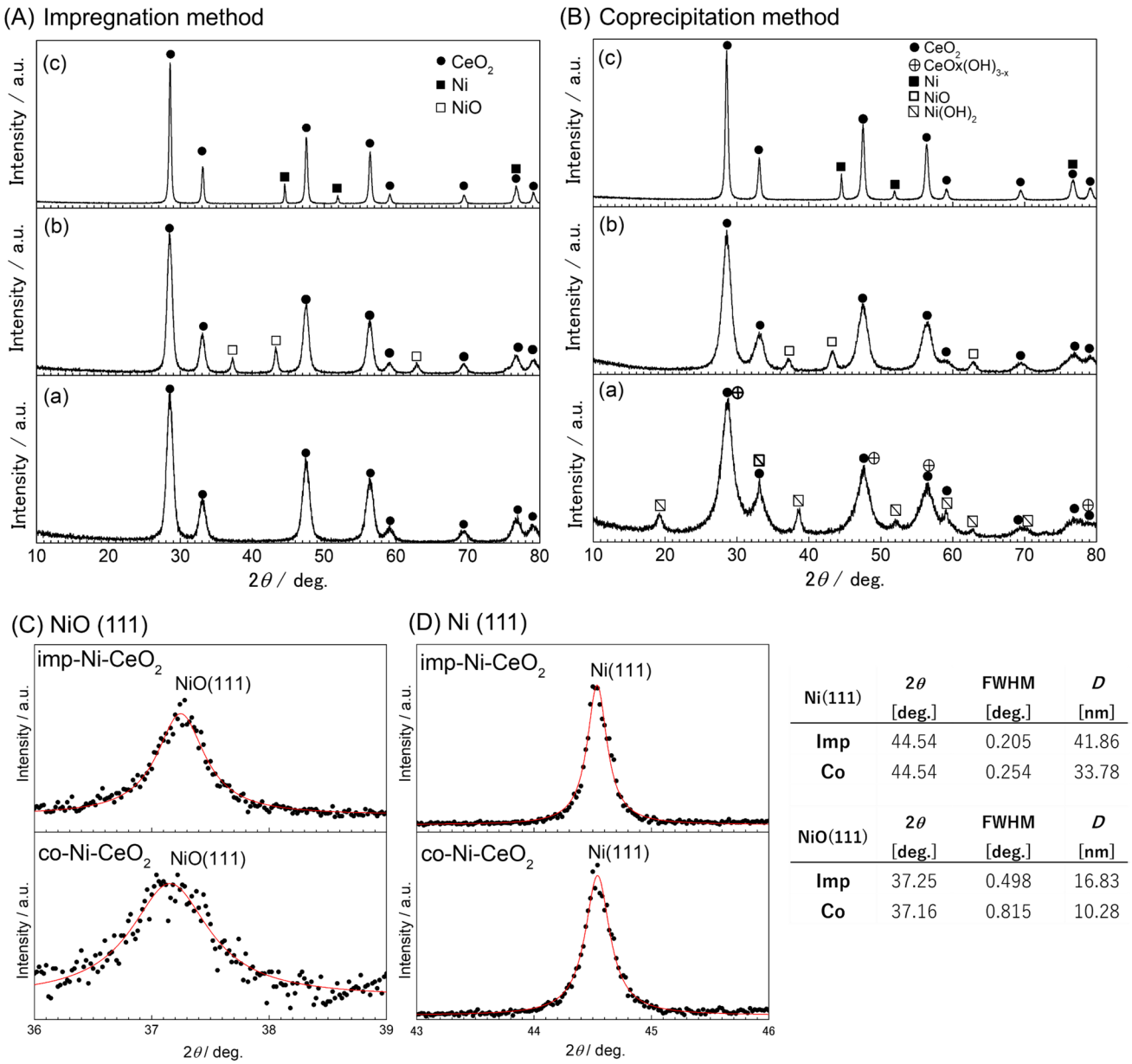

Ni(111)	2θ [deg.]	FWHM [deg.]	D [nm]
Imp	44.54	0.205	41.86
Co	44.54	0.254	33.78

NiO(111)	2θ [deg.]	FWHM [deg.]	D [nm]
Imp	37.25	0.498	16.83
Co	37.16	0.815	10.28

Fig. 1 XRD patterns recorded during the preparation of Ni–CeO_2 catalysts by impregnation (**A**) and coprecipitation (**B**), and profiles of NiO (111) (**C**) and Ni (111) (**D**) reflections for imp-Ni–CeO_2 and co-Ni–CeO_2 catalysts. Accompanying table summarizes diffraction angles, full width at half maximum (FWHM), and crystallite sizes for NiO (111) and Ni (111). (**A**) CeO_2 after initial preparation (**a**), after impregnation with $Ni(NO_3)_2$ solution and calcination at 500 °C (**b**), and after reduction at 600 °C under H_2 (imp-Ni–CeO_2) (**c**). (**B**) Coprecipitated precursor after drying at 100 °C (**a**), after calcination at 500 °C (**b**), and after reduction at 600 °C under H_2 (co-Ni–CeO_2) (**c**). (**C**, **D**) Experimental data are shown as dots; solid red lines represent Lorentzian fitting curves

precipitation of $Ce(OH)_3$ and $Ni(OH)_2$ caused by the large difference in their solubility products (K_{sp}). The reported K_{sp} values at 20 °C are 6.3×10^{-24} for $Ce(OH)_3$ [18] and 5.47×10^{-16} for $Ni(OH)_2$ [19], indicating that the K_{sp} of $Ni(OH)_2$ is approximately eight orders of magnitude larger than that of $Ce(OH)_3$.

Pore size distribution plots for CeO_2, co-Ni–CeO_2, and imp-Ni–CeO_2, and the surface areas are shown in Fig. 2C. All samples exhibit predominantly mesoporous structures. For CeO_2, the mesopores are mainly attributed to interparticle voids formed during the aggregation of primary particles. Compared with CeO_2, imp-Ni–CeO_2 exhibits a pronounced shift of the pore size distribution toward larger pore diameters, accompanied by a decrease in surface area. This behavior is attributed to impregnation of the as-prepared CeO_2 particles with a strongly acidic aqueous nickel nitrate

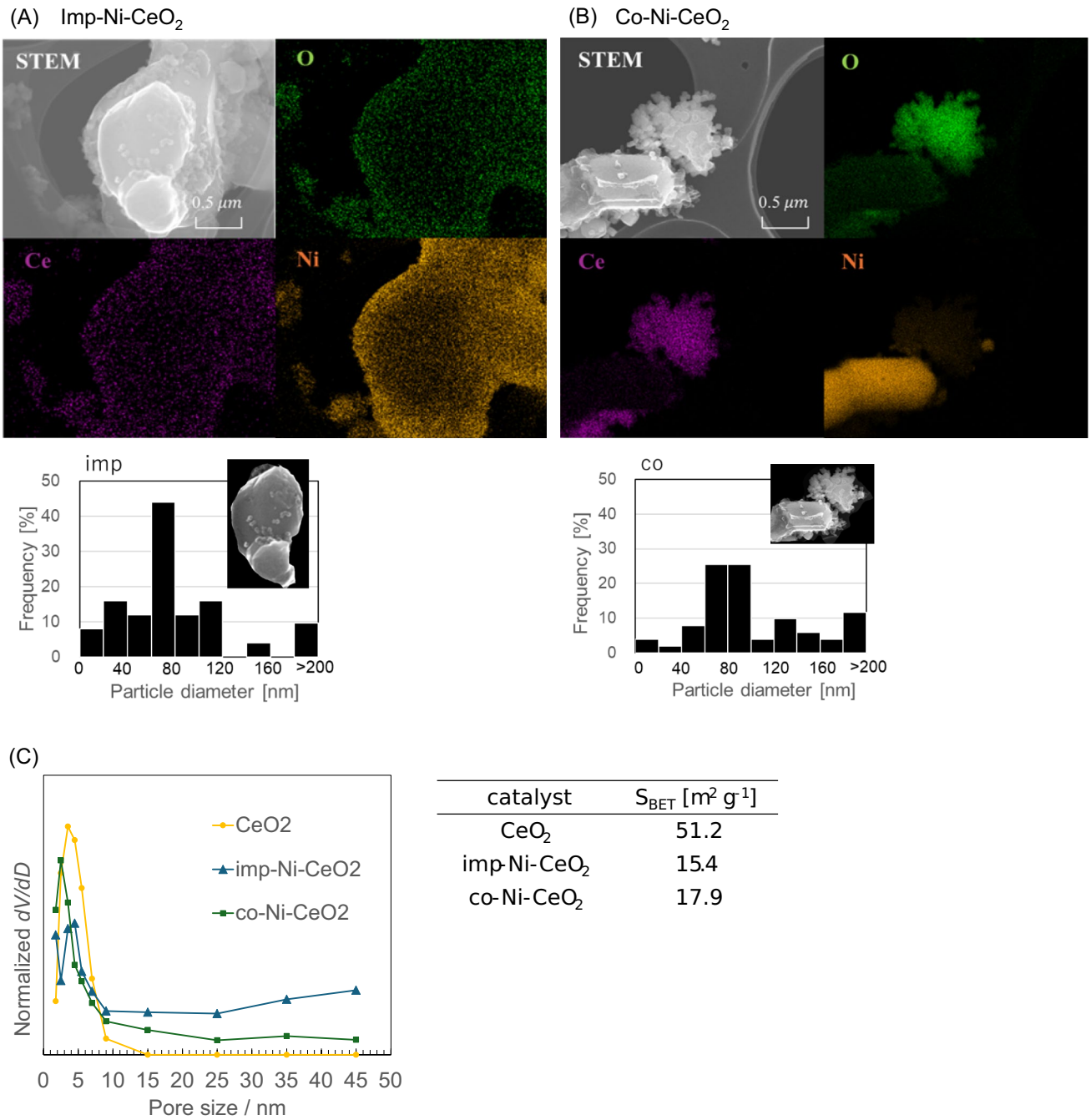

catalyst	S_{BET} [m^2 g^{-1}]
CeO_2	51.2
imp-Ni-CeO_2	15.4
co-Ni-CeO_2	17.9

Fig. 2 STEM images, corresponding EDX elemental maps, and the size histograms of imp-Ni–CeO_2 (**A**) and co-Ni–CeO_2 (**B**), showing the spatial distribution of Ce, Ni, and O within catalyst particles. (**C**) Pore size distributions derived from N_2 adsorption measurements for CeO_2 (yellow), imp-Ni–CeO_2 (navy), and co-Ni–CeO_2 (green) and the table of surface areas

solution, which may induce partial dissolution of CeO_2 in addition to adsorption of Ni species, resulting in reconstruction of the original CeO_2 particle morphology. Subsequent drying and calcination are expected to promote particle growth, leading to larger particle sizes for imp-Ni–CeO_2 relative to pristine CeO_2, thereby increasing pore diameters and reducing the surface area. In addition, partial blockage of CeO_2 pores by Ni species may contribute to the apparent decrease in the fraction of pores smaller than 10 nm. In contrast, co-Ni–CeO_2 shows a broader pore size distribution than CeO_2. As indicated by the results in Fig. 2B, regions where Ce and Ni species are homogeneously mixed are likely composed mainly of aggregates of relatively small primary particles formed through coprecipitation of Ce and Ni species. At the same time, localized Ni-rich regions are also observed, which are presumed to arise from sequential

precipitation of different hydroxides due to differences in solubility products, resulting in the formation of Ni-rich particles. According to SEM observations, these Ni-rich particles exceed 100 nm in size and are considered to be one of the factors contributing to the broadening of the pore size distribution.

Chemical states of catalyst surfaces

Figure 3A shows the Ni $2p_{3/2}$ X-ray photoelectron spectra for imp-Ni–CeO_2 and co-Ni–CeO_2, resolved into peaks corresponding to Ni^0, Ni^{2+}, and Ni^{2+} satellites [20, 21]. XRD analysis detected no crystalline NiO in either catalyst, suggesting that Ni–O bonds may exist within the CeO_2 lattice or as amorphous NiO. The ratio of metallic Ni on the surface, calculated as $Ni^0/(Ni^0 + Ni^{2+})$, was 0.576 for imp-Ni–CeO_2 and 0.463 for co-Ni–CeO_2, indicating that impregnation yields a higher fraction of exposed metallic Ni.

Figure 3B presents Ce 3d spectra for both catalysts. Peaks labeled u and v correspond to the Ce $3d_{3/2}$ and $3d_{5/2}$, respectively. Six peaks (v: 882.0 eV, v'': 888.4 eV, v''': 898.3 eV, u: 900.7 eV, u": 906.4 eV, u''': 916.4 eV) originate from Ce^{4+} [22], while four peaks (v_0: 880.6 eV, v': 884.5 eV, u_0: 902.5 eV, u': 898.9 eV) correspond to Ce^{3+}. The $Ce^{3+}/(Ce^{3+} + Ce^{4+})$ ratio, representing surface oxygen vacancy concentration, was 0.339 for imp-Ni–CeO_2 and 0.352 for co-Ni–CeO_2. Oxygen vacancies act as catalytic active sites for the adsorption of CO_2. This difference may affect the amount of CO_2 adsorption under the process of methanation. The metallic Ni-to-Ce ratio, based on peak areas, was 0.092 for imp-Ni–CeO_2 and 0.123 for co-Ni–CeO_2. STEM–EDX images of co-Ni–CeO_2 reveal large particles enriched in Ni species. The presence of O within these particles indicates that metallic Ni and nickel oxide are likely mixed. Such surface-exposed particles are more easily detected by XPS, which may explain the higher apparent metallic Ni concentration observed for co-Ni–CeO_2 relative to imp-Ni–CeO_2.

Methanation activity of the catalysts

The CO_2 methanation performance of imp-Ni–CeO_2 and co-Ni–CeO_2 was evaluated. Figure 4 shows CO_2 conversion and CH_4 selectivity as functions of temperature. For both catalysts, CO_2 conversion increased with temperature, with the most pronounced rise between 250 and 300 °C, followed by minimal changes at higher temperatures. CH_4 selectivity was similar for both catalysts up to 300 °C but increased significantly for imp-Ni–CeO_2 above 350 °C. Here, the apparent turnover frequency (TOF_{app}) at each temperature was calculated using the fraction of metallic Ni determined by XPS, together with the CO_2 conversion and CH_4 selectivity values. The results are summarized in Table 1.

Overall, the TOF_{app} values are estimated to be extremely small, which may be attributed to the assumption that all metallic Ni species identified by XPS, relative to the total amount of Ni introduced during catalyst synthesis, act as catalytically active sites. The TOF_{app} results suggest that co-Ni–CeO_2 exhibits relatively higher activity in the low-temperature region below 300 °C, whereas imp-Ni–CeO_2 tends to show higher activity at temperatures above 350 °C. Because both the surface area and the concentration of oxygen vacancies in CeO_2 are higher for co-Ni–CeO_2, enhanced

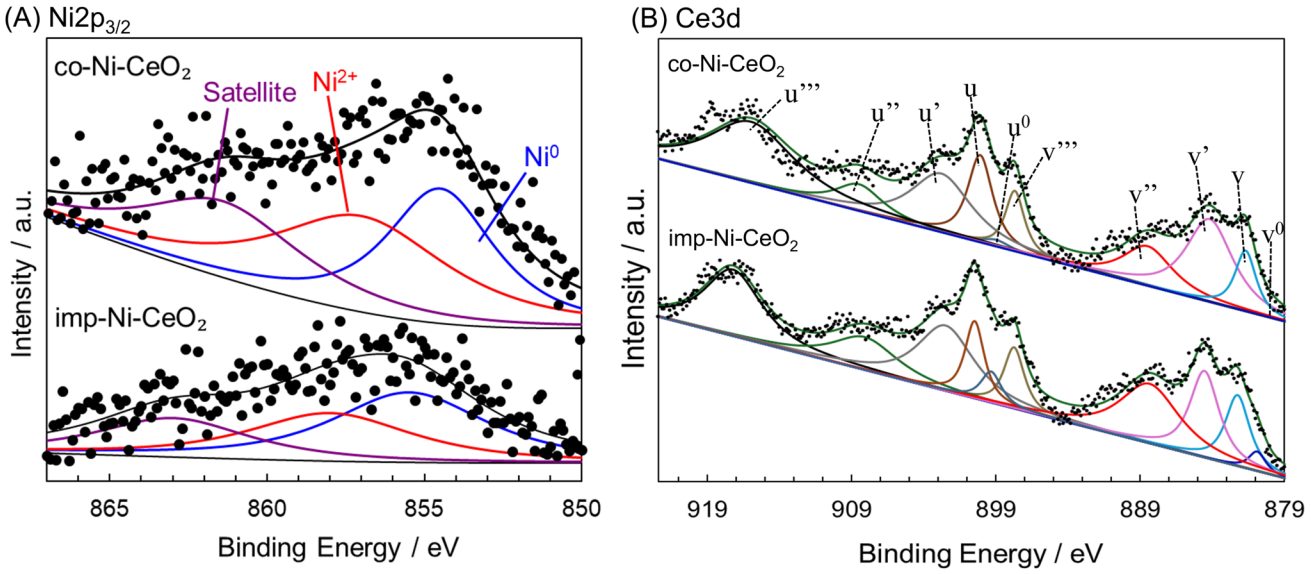

Fig. 3 Ni$2p_{3/2}$ and Ce3d X-ray photoelectron spectra of imp-Ni–CeO_2 and co-Ni–CeO_2 catalysts. Experimental data are shown as dots; solid lines represent the overall fitted curve and the individual peak components obtained from its deconvolution

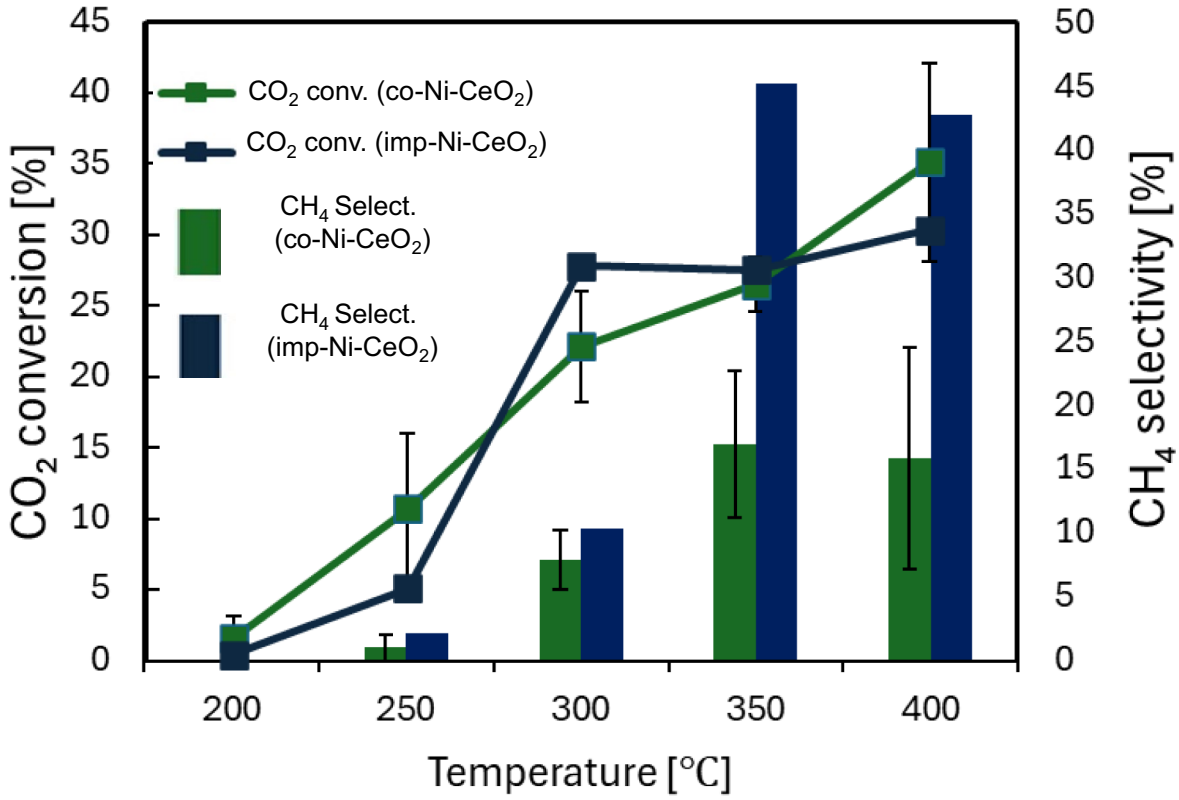

Fig. 4 Temperature dependence of CO_2 conversion and CH_4 selectivity for imp-Ni–CeO_2 and co-Ni–CeO_2 catalysts. CO_2 conversion is shown as a line graph with markers, while CH_4 selectivity is represented by bars. Colors: imp-Ni–CeO_2 (navy), co–Ni–CeO_2 (green). For the co–Ni–CeO_2, data represent the average of two runs, with error bars indicating the maximum and minimum values

Table 1 Apparent turnover frequency (TOF_{app})

	TOF_{app} [s^{-1}]	
	Imp-Ni–CeO_2	Co–Ni–CeO_2
200 °C	0	0
250 °C	5.82×10^{-7}	6.52×10^{-6}
300 °C	1.42×10^{-5}	3.31×10^{-5}
350 °C	5.63×10^{-5}	4.06×10^{-5}
400 °C	5.47×10^{-5}	3.33×10^{-5}

CO_2 adsorption in the low-temperature region below 300 °C cannot be excluded. Oxygen vacancies in CeO_2 are known to function as Lewis acid sites for CO_2 activation and are suggested to promote CO_2 adsorption and conversion [23]. In addition, co-Ni–CeO_2 consists not only of agglomerates of particles smaller than 100 nm, in which Ni, Ce, and O species are uniformly distributed, but also of larger particles in which Ni species are locally enriched. These larger particles may possess a relatively high density of Ni active sites and may therefore act as hydrogenation sites for CO and CH_4 species even at low temperatures. This structural feature may contribute to the apparently higher TOF_{app} observed for co-Ni–CeO_2 compared with imp-Ni–CeO_2 in the low-temperature region. In contrast, the higher TOFapp observed for imp-Ni–CeO_2 at elevated temperatures may be attributed to the relaxation of kinetic limitations, under which a larger fraction of the catalyst surface becomes active [24]. Under such conditions, both CO_2 adsorption sites and Ni active sites are more widely accessible, leading to enhanced overall catalytic activity.

The catalyst materials synthesized in this study exhibit higher optimal reaction temperatures and lower CO_2 conversion and CH_4 selectivity at 400 °C compared with previously reported Ni–CeO_2 catalysts, such as those described by Rui et al [10] and Chen et al. [13]. These earlier studies suggest that the use of plasma treatments or controlled atmospheres during catalyst calcination enables the effective refinement of Ni particles to sizes below 10 nm, enhances the dispersion of Ni on CeO_2, and promotes the formation of interfacial structures arising from strong interactions between Ni and oxygen vacancies in CeO_2. In our system, the lower CO_2

conversion is primarily attributed to the relatively small surface area available for gas adsorption. Both imp-Ni–CeO_2 and co-Ni–CeO_2 exhibit particle size distributions with a dominant volume range of 60–100 nm, which is larger than those reported in the literature, inevitably resulting in lower surface areas. In addition, for co-Ni–CeO_2, the relatively low dispersion of Ni leads to a reduced interfacial density between Ni and CeO_2, which also contributes to the reduced activity. CO_2 adsorbed near the Ni–CeO_2 interface has a lower probability of encountering hydrogen adsorbed on Ni when metallic Ni sites are sparsely distributed. As a result, both CO_2 conversion and CH_4 selectivity are expected to decrease.

Conclusion

In this study, the morphological and chemical-state differences of Ni–CeO_2 catalysts prepared by coprecipitation and impregnation were elucidated using XRD, STEM-EDX, and XPS analyses, and their effects on CO_2 methanation were discussed based on the apparent turnover frequency (TOF_{app}). For the catalysts prepared by coprecipitation, particles smaller than 100 nm with a uniform distribution of Ce, Ni, and O species were observed. At the same time, large bulk-like particles with pronounced localization of Ni species were also formed, which is likely attributable to the large difference in the solubility products of cerium hydroxide and nickel hydroxide during the synthesis process. In contrast, for the impregnation-derived catalysts, structures were observed in which particles smaller than 100 nm were attached to extremely large particles exceeding 500 nm. Nevertheless, a uniform distribution of Ce, Ni, and O species was confirmed regardless of particle size.

The surface area and oxygen vacancy concentration, both of which influence CO_2 adsorption, were slightly higher for the coprecipitation-derived catalysts. This difference is one of the factors responsible for the higher TOF_{app} values estimated for co-Ni–CeO_2 compared with imp-Ni–CeO_2 in the low-temperature region below 300 °C. In addition, the large particles with localized Ni species are thought to possess a high density of metallic Ni active sites and may therefore function as hydrogenation sites for CO and CH_4 species even at low temperatures. This feature is another factor contributing to the higher TOF_{app} values of co-Ni–CeO_2 relative to imp-Ni–CeO_2 in the low-temperature region. In the high-temperature region above 350 °C, CH_4 selectivity was markedly higher for the catalysts prepared by impregnation, and the TOF_{app} values were also higher for imp-Ni–CeO_2. This behavior is attributed to the alleviation of kinetic limitations at elevated temperatures, under which the entire catalyst becomes activated due to the widespread availability of both CO_2 adsorption sites and Ni active sites.

Based on the results obtained in this study, it is evident that additional processes are required, including particle size reduction or the formation of porous structures to increase surface area, the creation of surfaces rich in oxygen vacancies, and the deliberate formation of interfaces where CO_2 adsorption sites and hydrogen activation sites are located in close proximity.

Acknowledgments This work was supported by JSPS KAKENHI (Grant Number JP25K08290), the JSPS Program for Forming Japan's Peak Research Universities (J-PEAKS, Grant Number JPJS00420230010), and partially by the "Initiative for Realizing Diversity in the Research Environment" from MEXT. NF acknowledges Dr. H. Watanabe and T. Okada of AIST Chugoku for their assistance with XPS measurements and analysis. We also thank Dr. C. Nakano at Division of Instrumental Analysis in Okayama University for support with STEM observations. Finally, we express our sincere gratitude to Prof. Uddin MD. Azhar for his valuable advice on catalyst performance evaluation.

Author contributions All authors contributed to the study conception and design. Catalyst preparation, data collection, and analysis were performed by Nobuko Fukuda and Shuichi Imano. Nozomi Nakahara supervised methanation tests using gas chromatography. The first draft of the manuscript was written by Nobuko Fukuda, and all authors read and approved the final manuscript.

Funding Open Access funding provided by Okayama University. This work was supported in part by JSPS KAKENHI (Grant Number JP25K08290), JSPS Program for Forming Japan's Peak Research Universities (J-PEAKS, Grant Number JPJS00420230010), and the "Initiative for Realizing Diversity in the Research Environment" from MEXT.

Data availability The data that support the findings of this study are available on request from the corresponding author.

Declarations

Conflict of interest Authors declare that this study was conducted without any commercial or financial relationships that could be construed as a potential conflict of interest.

References

1. S. Rönsch, J. Schneider, S. Matthischke, M. Shlüter, M. Götz, J. Lefebvre, P. Prabhakaran, S. Bajohr, Fuel **166**, 276–296 (2016). https://doi.org/10.1016/j.fuel.2015.10.111
2. J.B. Powell, S.H. Langer, J. Catal. **94**, 566–569 (1985). https://doi.org/10.1016/0021-9517(85)90222-2
3. G.A. Mills, F.W. Steffgen, Catal. Rev. **8**, 159–210 (1974). https://doi.org/10.1080/01614947408071860
4. J. Gao, Q. Liu, F. Gu, B. Liu, Z. Zhong, F. Su, RSC Adv. **5**, 22759–22776 (2015). https://doi.org/10.1039/C4RA16114A
5. G. Vilé, S. Colussi, F. Krumeich, A. Trovarelli, Angew. Chem. **126**, 12265–12268 (2014). https://doi.org/10.1002/ange.201406637
6. F.M. Monta, D.H. Kim, Chem. Soc. Rev. **48**, 205–209 (2019). https://doi.org/10.1016/j.jcat.2024.115778
7. A. Cárdenas-Arenas, A. Quindimil, A. Davó-Quinonero, E. Bailón-Garcíaa, D. Lozano-Castellóa, U. De-La-Torre, B. Pereda-Ayo, J.A. González-Marcos, J.R. González-Velasco, A. Bueno-López, Appl. Mater. Today **19**, 100591 (2020). https://doi.org/10.1016/j.apmt.2020.100591
8. S. Ullah, S.M. Ahmed, T. Huang, Y. Pan, Z. Yu, Q. Xue, R. Ye, Z. Wang, S. Kawi, Y. Wang, G. Luo, Chem. Eng. J. **515**, 163859 (2025). https://doi.org/10.1016/j.cej.2025.163859
9. N. Rui, X. Zhang, F. Zhang, Z. Liu, X. Cao, Z. Xie, R. Zou, S.D. Senanayake, Y. Yang, J.A. Rodriguez, C.-J. Liu, Appl. Catal. B Environ. **282**, 119581 (2021). https://doi.org/10.1016/j.apcatb.2020.119581
10. Y. Zhang, T. Zhang, F. Wang, Q. Zhu, Q. Liu, Greenhouse Gases Sci. Technol. **11**, 1222–1233 (2021). https://doi.org/10.1002/ghg.2121
11. A. Cárdenas-Arenas, A. Quindimil, A. Davó-Quiñonero, E. Bailón-García, D. Lozano-Castelló, U. De-La-Torre, B. Pereda-Ayo, J.A. González-Marcos, J.R. González-Velasco, A. Bueno-López, Appl. Catal. B **265**, 118538 (2020). https://doi.org/10.1016/j.apcatb.2019.118538
12. S. Tada, H. Nagase, N. Fujiwara, R. Kikuchi, Energy Fuels **35**, 5241–5251 (2021). https://doi.org/10.1021/acs.energyfuels.0c04238
13. S. Chen, L. Higgins, I. Giarnieri, P. Benito, A.M. Beale, J. Catal. **439**, 115778 (2024). https://doi.org/10.1016/j.jcat.2024.115778
14. W. She, T. Qi, M. Cui, P. Yan, S.W. Ng, W. Li, G. Li, ACS Appl. Mater. Interfaces **10**, 14698–14707 (2018). https://doi.org/10.1021/acsami.8b01187
15. X. Liao, Y. Zhang, M. Hill, X. Xia, Y. Zhao, Z. Jiang, Appl. Catal. A Gen. **488**, 256–264 (2014). https://doi.org/10.1016/j.apcata.2014.09.042
16. Y. Malyukin, V. Klochkov, P. Maksimchuk, V. Seminko, N. Spivak, Nanoscale Res. Lett. **12**, 566 (2017)
17. R.F. André, G. Rousse, C. Sassoye, M. Avdeev, B. Lassalle-Kaiser, B. Baptiste, S. Carenco, Chem. Mater. **35**, 5040–5048 (2023). https://doi.org/10.1021/acs.chemmater.3c00486
18. H.-I. Chen, H.-Y. Chang, Colloids. Surf. A-Physicochem. Eng. Asp. **242**, 61–69 (2004). https://doi.org/10.1016/j.colsurfa.2004.04.056
19. K. Provazi, M.J. Giz, L.H. Dall'Antonia, S.I. Córdoba de Torresi, J. Power. Sources **102**, 224–232 (2001). https://doi.org/10.1016/S0378-7753(01)00819-9
20. M.A. Peck, M.A. Langell, Chem. Mater. **24**, 4483–4490 (2012). https://doi.org/10.1021/cm300739y
21. L. Xu, C. Xu, B. Chen, Y. Bian, X. Wen, G. Cheng, C.-e Wu, J. Qiu, M. Chen, Fuel **333**, 126411 (2023). https://doi.org/10.1016/j.fuel.2022.126411
22. A. Buhori, J.-W. Choi, H. Jee, C.S. Kim, K.H. Kim, K. Kim, W. Yang, J.-M. Ha, C.-J. Yoo, Chem. Eng. J. **499**, 156097 (2024). https://doi.org/10.1016/j.cej.2024.156097
23. C. Zhu, X. Wei, W. Li, Y. Pu, J. Sun, K. Tang, H. Wan, C. Ge, W. Zou, L. Dong, ACS Sustain. Chem. Eng. **8**, 14397–14406 (2020). https://doi.org/10.1021/acssuschemeng.0c04205
24. Y. Guo, S. Mei, K. Yuan, D.-J. Wang, H.-C. Liu, C.-H. Yan, Y.-W. Zhang, ACS Catal. **8**, 6203–6215 (2018). https://doi.org/10.1021/acscatal.7b04469